

A unified bounding surface plasticity model for unsaturated soils

A. R. Russell¹ and N. Khalili^{2,*†}

¹ *Department of Civil Engineering, University of Bristol, Queens Building, University Walk, Bristol, BS8 1TR, U.K.*

² *School of Civil and Environmental Engineering, University of New South Wales, Sydney, NSW 2052, Australia*

SUMMARY

A unified constitutive model for unsaturated soils is presented in a critical state framework using the concepts of effective stress and bounding surface plasticity theory. Consideration is given to the effects of unsaturation and particle crushing in the definition of the critical state. A simple isotropic elastic rule is adopted. A loading surface and a bounding surface of the same shape are defined using simple and versatile functions. The bounding surface and elastic rules lead to the existence of a limiting isotropic compression line, towards which the stress trajectories of all isotropic compression load paths approach. A non-associated flow rule of the same general form is assumed for all soil types. Isotropic hardening/softening occurs due to changes in plastic volumetric strains as well as suction for some unsaturated soils, enabling the phenomenon of volumetric collapse upon wetting to be accounted for. The model is used to simulate the stress–strain behaviour observed in unsaturated speswhite kaolin subjected to three triaxial test load paths. The fit between simulation and experiment is improved compared to that of other constitutive models developed using conventional Cam-Clay-based plasticity theory and calibrated using the same set of data. Also, the model is used to simulate to a high degree of accuracy the stress–strain behaviour observed in unsaturated Kurnell sand subjected to two triaxial test load paths and the oedometric compression load path. For oedometric compression theoretical simulations indicate that the suction was not sufficiently large to cause samples to separate from the confining ring. Copyright © 2005 John Wiley & Sons, Ltd.

KEY WORDS: unsaturated; sand; clay; bounding surface; plasticity; suction; hardening; effective stress

1. INTRODUCTION

Unsaturated soils are combinations of three phases: solid particles, air and water occupying the pore space. Their stress–strain behaviour is complex and is influenced by many factors including externally applied stresses, soil type, structure, density, and suction arising from surface tension across the air–water interface within the soil. Most notably, suction increases the shear strength,

*Correspondence to: N. Khalili, School of Civil and Environmental Engineering, University of New South Wales, Sydney, NSW 2052, Australia.

†E-mail: n.khalili@unsw.edu.au

and stiffens the soil skeletal response. Upon wetting, however, this increase in the stiffness of the soil skeleton is lost and may be associated with large and non-reversible volumetric collapse of the soil structure. Unsaturated soils are widely spread and these behavioural characteristics need to be dealt with in many engineering problems including foundations, pavements, natural and made slopes.

Several constitutive models have been developed for unsaturated fine-grained soils (such as silts and clays) using extensions of Cam-Clay-type models in a critical state framework. The models of Alonso *et al.* [1], Wheeler and Sivakumar [2] and Cui and Delage [3] are similar and treat suction and externally applied stress as independent stress variables. It was necessary to introduce a load-collapse curve to account for the effects of suction. Many of the material parameters, including those that define the critical state, were suction dependant making the laboratory testing required to calibrate the models time consuming. These models capture many of the behavioural characteristics of unsaturated soils, including the dependence of the size of yield surface on suction and volumetric collapse upon wetting, and simulate the stress-strain behaviour of some laboratory test results reasonably well. However, they fail to reproduce the elastic response that follows the plastic response in isotropically compressed soils subject to increasing suction. No such problem surrounds the constitutive model of Loret and Khalili [4], in which suction was combined with externally applied stress into a single-stress variable termed the *effective stress*. This work, and that of Gallipoli *et al.* [5], overcame one of the challenges facing this approach in that volumetric collapse upon wetting could be modelled. In comparison, much less attention has been given to the constitutive modelling of unsaturated coarse-grained soils (such as sands) despite suction having a significant affect on their stress-strain behaviour [6–8]. One model is reported by Rampino *et al.* [9] where the model of Jefferies [10] was adapted using many of the features of Alonso *et al.* [1] to match the observed stress-strain behaviour of an unsaturated silty sand. Reasonable predictions were found for some laboratory test results, while others were not predicted at all well.

The aim of this paper is to develop a constitutive model that is sufficiently general such that it is suited to a wide range of unsaturated soils. The model is formulated using bounding surface plasticity theory, due to its versatility [11] and ability to accurately reproduce the stress-strain behaviour of many soil types to good accuracy [12, 13], and is an extension of that proposed by Russell and Khalili [14]. It is presented in a critical state framework using the concept of effective stress. The advantage of using the effective stress is that the elastic deformation as well as the *limiting* shear strength of the soil can completely be expressed in terms of a single ‘effective’ stress rather than two or three independent stress variables [15]. Both pre- and post peak plasticity are taken into account. A non-associated flow rule is adopted and the isotropic hardening/softening of the soil matrix is related to a change in suction as well as plastic volumetric strain. Consideration is given to the effects of unsaturation in the definition of the critical state and also to the effects of particle crushing in sands at high stresses. For simplicity, triaxial notations are adopted and hydraulic hysteresis and time dependant phenomena are ignored.

The model is calibrated for speswhite kaolin using the triaxial compression test results for three load paths presented in Reference [2]; and for Kurnell sand, a predominantly quartz sand containing no fines, using the triaxial compression and oedometric compression test results reported in Reference [16].

2. EFFECTIVE STRESS

Defined as a combination of the total stress and pore pressures, the effective stress converts a multi-phase, multi-stress state porous medium to a *mechanically equivalent* single-phase, single-stress state continuum. This enables the application of the principles of continuum solid mechanics to fluid-filled deformable porous media [15]. The effective stress enters the elastic as well as elasto-plastic constitutive equations of the solid phase, although for the later it may also be accompanied by an additional stress variable, usually suction, to describe some aspects of hardening and softening. A change in effective stress is linked to straining or any other relevant quantity of the soil skeleton [4].

For unsaturated soils, the effective stress [17] is defined as

$$\boldsymbol{\sigma}' = \boldsymbol{\sigma}_n + \chi s \mathbf{I} \quad (1)$$

where $\boldsymbol{\sigma}'$ is the effective stress; $\boldsymbol{\sigma}_n$ is the total stress in excess of pore air pressure (u_a) also referred to as net stress; s is the difference between pore air and pore water pressure ($u_a - u_w$) also referred to as suction; and χ is the effective stress parameter attaining a value of 1 for saturated soils, and zero for dry soils. Khalili *et al.* [15] demonstrated application of the effective stress approach using strength and volume change data for a range of soil types from four different laboratories.

3. NOTATIONS

Conventional triaxial p' - q notation is used, where p' is the mean effective stress and q is the deviator stress. The corresponding work conjugate strain variables are the soil skeleton volumetric (isotropic) strain ε_p and shear (deviatoric) strain ε_q . They are related to axial and radial stresses and strains in the usual way, where

$$p' = \frac{\sigma'_1 + 2\sigma'_3}{3}, \quad q = \sigma'_1 - \sigma'_3, \quad \varepsilon_p = \varepsilon_1 + 2\varepsilon_3, \quad \varepsilon_q = \frac{2}{3}(\varepsilon_1 - \varepsilon_3) \quad (2)$$

and subscripts 1 and 3 denote the axial and radial components, respectively. Within this context, and by recognizing that χ deviates from S_r due to surface tension effects, the work conjugate for ns is S_r [18], where n is the porosity and S_r is the degree of saturation.

Compressive stresses and strains are assumed positive and volumetric strain is linked to specific volume (v) according to

$$\varepsilon_p = -\ln\left(\frac{v}{v_0}\right) \quad (3)$$

where $v = 1 + e$, e is the void ratio and v_0 is the specific volume at the reference configuration. In incremental form Equation (3) can be rewritten as

$$\dot{\varepsilon}_p = -\frac{\dot{v}}{v} \quad (4)$$

where a superimposed dot indicates an increment. Elastic and plastic strain increments sum to give total strain increments in the usual way:

$$\begin{bmatrix} \dot{\varepsilon}_p \\ \dot{\varepsilon}_q \end{bmatrix} = \begin{bmatrix} \dot{\varepsilon}_p^e \\ \dot{\varepsilon}_q^e \end{bmatrix} + \begin{bmatrix} \dot{\varepsilon}_p^p \\ \dot{\varepsilon}_q^p \end{bmatrix} \quad (5)$$

where the superscripts e and p denote the elastic and plastic components, respectively. The pairs of stresses and strains are abbreviated in vector form $\boldsymbol{\sigma} = [p', q]^T$ and $\boldsymbol{\varepsilon} = [\varepsilon_p, \varepsilon_q]^T$.

4. THE UNIFIED BOUNDING SURFACE PLASTICITY MODEL

4.1. General

Major attractions of bounding surface plasticity theory [11] are that it lends itself to a number of general and versatile formulations; each removing the abrupt change from elastic to elastic–plastic behaviour of typical models developed using the conventional plasticity theory.

The bounding surface plasticity model presented here is an extension of that appearing in Russell and Khalili [14], and was initially developed to describe the stress–strain behaviour of a saturated quartz sand across a range of stresses including those sufficient to cause particle crushing and subjected to varied load paths. However, the underlying features of the model are sufficiently general such that it is also suited to describe the stress–strain behaviour of a wide range of unsaturated soils and is the focus of this investigation.

4.2. Stress–strain relationships

The effective stress stems from elastic (mechanical) straining of the soil skeleton. It follows that incremental elastic strains are linked to the incremental stress invariant through:

$$\dot{\boldsymbol{\sigma}} = \mathbf{D}^e \dot{\boldsymbol{\varepsilon}}^e \quad (6)$$

where \mathbf{D}^e is the elastic stiffness matrix. No further restriction is placed on the effective stress. In fact, the plastic stress–strain relationship may include a suction dependence as well as an effective stress dependence without violating the concept of effective stress. It is written in the general form:

$$\dot{\boldsymbol{\varepsilon}}^p = \frac{1}{h} (\mathbf{n}^T \dot{\boldsymbol{\sigma}}) \mathbf{m} \quad (7)$$

where $\mathbf{n} = [n_p, n_q]^T$ is the unit normal vector at the current stress state on the loading surface controlling the direction of loading, $\mathbf{m} = [m_p, m_q]^T$ is the unit direction of plastic flow at the current stress state and h is the hardening modulus.

The elastic–plastic stress–strain relationship is obtained by combining Equations (5), (6) and (7) and is of the form

$$\dot{\boldsymbol{\sigma}} = \left(\mathbf{D}^e - \frac{\mathbf{D}^e \mathbf{m} \mathbf{n}^T \mathbf{D}^e}{h + \mathbf{n}^T \mathbf{D}^e \mathbf{m}} \right) \dot{\boldsymbol{\varepsilon}} \quad (8)$$

4.3. The critical state

The critical state acts as a reference condition towards which all states approach with increasing plastic shear strain. The critical state therefore has an important role in the model and consideration must be given to the effects of unsaturation in its definition.

It is often assumed that the critical state line (CSL) is straight in the v – $\ln p'$ and q – p' planes for both saturated sands and clays. However, there is experimental evidence that the CSL for sands in the v – $\ln p'$ plane may not be straight as it is affected by particle crushing

at high stresses [19, 20]. In this study the CSL for saturated sands is assumed to take the form of three linear segments (illustrated in Figure 1) as identified by Russell and Khalili [21] through a review of several sets of experimental data across a wide stress range. The three linear segments are defined by the six material parameters λ_0 , Γ_0 , v_{cr} , λ_{cr} , v_f and λ_f . λ_0 and Γ_0 are the slope of the initial portion of the CSL and its specific volume at $p' = 1$ kPa, respectively; v_{cr} is the specific volume at the onset of particle crushing; λ_{cr} is the slope during the particle crushing stage; and v_f and λ_f are the specific volume at the end of crushing and the slope of the CSL at extremely high stresses, respectively. A smooth equation that closely fits the three linear segments was proposed by Russell and Khalili [14] and details are given in Appendix A.

The experimental data presented in References [2, 3, 5] for saturated and unsaturated soils when interpreted in an effective stress framework provides evidence that s influences the location of CSL in the v – $\ln p'$ plane. Loret and Khalili [4, 22] attributed this response to suction hardening, an isotropic hardening phenomenon that controls the size of the yield surface (when using conventional plasticity theory) in addition to plastic volumetric strains, and therefore the location of the CSL.

For saturated conditions a general definition of the CSL in the v – p' plane is adopted in the model formulation for simplicity:

$$v = f_{cs}(p') \quad (9a)$$

where f_{cs} is a function unique to a given soil. General definition of the CSL in the v – p' for unsaturated conditions thus takes the form

$$v = \hat{f}_{cs}(p', s) \quad (9b)$$

The CSL in the q – p' plane will now be discussed. For saturated clays there is much experimental evidence that the stress ratio ($\eta = q/p'$) approaches a constant value at large shear strains in triaxial tests, and therefore the CSL is linear and passes through the origin. Adopting the

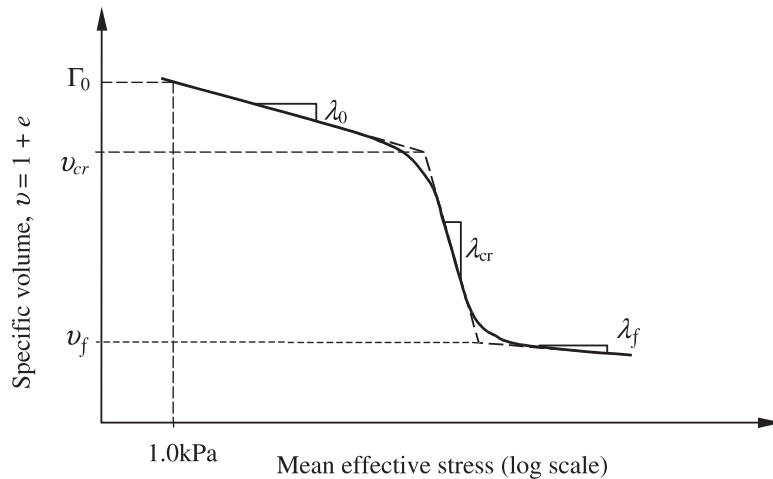


Figure 1. A general critical state line for saturated sands in the v – $\ln p'$ plane.

Mohr–Coulomb failure criterion it can be shown that at the slope of the CSL (M_{cs}) is simply a function of the critical state friction angle (ϕ'_{cs}) according to:

$$M_{cs} = \eta = \frac{6 \sin \phi'_{cs}}{3t - \sin \phi'_{cs}} \quad (10)$$

where M_{cs} and ϕ'_{cs} are material constants, $t = +1$ for compressive loading ($q > 0$) and $t = -1$ for extensive loading ($q < 0$).

For saturated quartz sands Lo and Roy [23], Lade [24], Colliat-Dangus *et al.* [25], Yamamuro and Lade [26] and Russell and Khalili [14] showed that the stress ratio also approaches a constant value at large shear strains for stresses ranging from 50 to 15 000 kPa. Therefore, it is assumed here that the slope of the CSL in the q – p' plane is also a material constant, irrespective of the amount of particle crushing that the sand may have experienced. Equation (10) therefore also applies. There is some evidence, however, that for saturated calcareous sands ϕ'_{cs} is dependant on grain size, and therefore particle crushing [23, 25].

Furthermore, Khalili *et al.* [15] reviewed triaxial compression test data for several saturated and unsaturated soils from four different laboratories. Application of the effective stress approach was demonstrated and, by adopting an appropriate relationship for χ , ϕ'_{cs} and M_{cs} were found to be material constants for saturated and unsaturated conditions.

4.4. Elasticity

A simple isotropic elastic rule is adopted and is the same as that used for both sands and clays in other constitutive models. The existence of a purely elastic region is ignored such that all deformation is elastic–plastic, the soil is always at yield and the current stress state always lies on the loading surface. This is in general agreement with experimental evidence for sands where truly elastic behaviour was observed to end at shear strains in the order of 0.00001 [27]. Also, the hysteresis commonly observed in unload–reload cycles of clays (Figures 3.12 and 3.13 of Reference [28]) suggests that deformation is not purely elastic. Another advantage of the non-existence of a purely elastic region is that the non-vertical response of undrained triaxial test results when plotted in the q – p' plane can be modelled.

Specifically, incremental elastic volumetric strain accompanies a change in p' according to a linear relationship between v and $\ln p'$ such that the elastic bulk modulus K (appearing in \mathbf{D}^e) is defined as

$$K = \frac{vp'}{\kappa} \quad (11)$$

where κ is a material constant. For triaxial conditions the elastic shear modulus G (also appearing in \mathbf{D}^e) is then defined as

$$G = \frac{3(1 - 2v)}{2(1 + v)} K \quad (12)$$

where v denotes Poisson's ratio and is assumed constant.

4.5. Loading surface, bounding surface and image point

The concept of a bounding surface first introduced by Dafalias and Popov [29] is applied here. Plastic deformation occurs when the current stress state, denoted using $\boldsymbol{\sigma}$ hereafter, lies on or within the bounding surface. This is achieved by defining the plastic modulus to be a decreasing

function of the distance between σ and an ‘image point’ on the bounding surface. The image point is denoted using $\bar{\sigma}$ hereafter, and a superimposed bar recognizes an association with the bounding surface.

For simplicity, a loading surface and bounding surface of the same shape and homologous about the origin in the q - p' plane are assumed. Also, a simple radial mapping rule is assumed such that a straight line that passes through the origin and σ intersects the bounding surface at $\bar{\sigma}$. It follows that the unit normal vectors of the loading surface and bounding surface at σ and $\bar{\sigma}$ are the same. Simple and versatile functions for the loading surface and bounding surface are adopted and are of the form $f(p', q, p'_c) = 0$ and $F(\bar{p}', \bar{q}, \bar{p}'_c) = 0$, with:

$$f(p', q, p'_c) = t \left\{ q - M_{cs} p' \left[\frac{\ln(p'_c/p')}{\ln R} \right]^{1/N} \right\} \quad (13a)$$

$$F(\bar{p}', \bar{q}, \bar{p}'_c) = t \left\{ \bar{q} - M_{cs} \bar{p}' \left[\frac{\ln(\bar{p}'_c/\bar{p}')}{\ln R} \right]^{1/N} \right\} \quad (13b)$$

where the parameters p'_c and \bar{p}'_c control the size of the loading surface and bounding surface, respectively, and represent intercepts with the $q = 0$ axis as illustrated in Figure 2. The material constant R represents the ratio between p' at the intercept of the loading surface with the M_{cs} line and p'_c , and the ratio between \bar{p}' at the intercept of the bounding surface with the M_{cs} line and \bar{p}'_c . Note that M_{cs} may be one of two constants in Equation (10), depending on whether compressive ($q > 0$) or extensive ($q < 0$) loading is occurring. The material constant N controls the curvature.

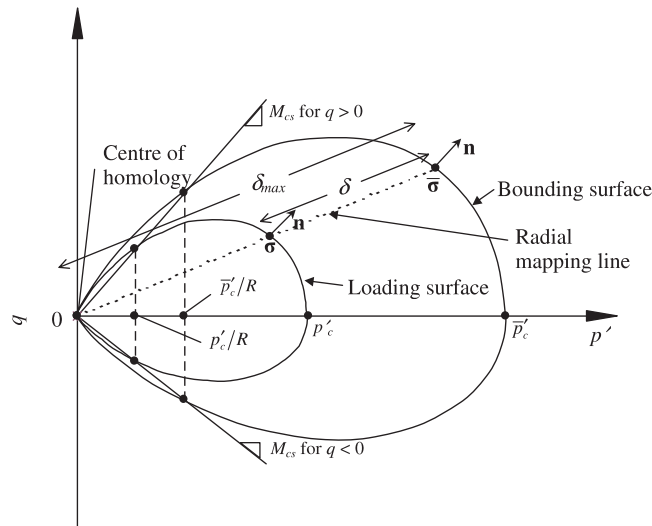


Figure 2. Loading surface, bounding surface and radial mapping line in the q - p' plane.

The unit normal vector at the image point defining the direction of loading is then

$$\mathbf{n} = \frac{\frac{\partial f}{\partial \bar{\sigma}}}{\left\| \frac{\partial f}{\partial \bar{\sigma}} \right\|} = \left[\frac{-t \frac{\bar{q}}{\bar{p}'} \left(1 - \frac{1}{N \ln(\bar{p}'_c / \bar{p}')} \right)}{\sqrt{\left(-\frac{\bar{q}}{\bar{p}'} \left(1 - \frac{1}{N \ln(\bar{p}'_c / \bar{p}')} \right) \right)^2 + 1}}, \frac{t}{\sqrt{\left(-\frac{\bar{q}}{\bar{p}'} \left(1 - \frac{1}{N \ln(\bar{p}'_c / \bar{p}')} \right) \right)^2 + 1}} \right]^T \quad (14a)$$

Note that due to the homotetic conditions \mathbf{n} may be expressed in terms of the stress invariants associated with the loading surface rather than the bounding surface as

$$\mathbf{n} = \frac{\frac{\partial f}{\partial \sigma}}{\left\| \frac{\partial f}{\partial \sigma} \right\|} = \left[\frac{-t \frac{q}{p'} \left(1 - \frac{1}{N \ln(p'_c / p')} \right)}{\sqrt{\left(-\frac{q}{p'} \left(1 - \frac{1}{N \ln(p'_c / p')} \right) \right)^2 + 1}}, \frac{t}{\sqrt{\left(-\frac{q}{p'} \left(1 - \frac{1}{N \ln(p'_c / p')} \right) \right)^2 + 1}} \right]^T \quad (14b)$$

Insight into suitable values of N and R for a given soil type are gained through the results of constant volume shear tests performed on samples when initially $p' = p'_c \cong \bar{p}'_c$. If the elastic strains are small then \bar{p}'_c does not change significantly during shearing and the stress trajectory in the q - p' plane closely follows the loading surface. The non-vertical response and various amounts of curvature and hook observed in saturated undrained triaxial test results performed on loose to medium dense sands in the q - p' plane can therefore be accounted for. Furthermore, shapes similar to the yield surfaces of Tatsuoka and Ishihara [30] and Nova and Wood [31] for sands are obtained by adopting a value of N larger than about 2. Also, a shape the same as the yield surface of Cam-Clay is obtained by adopting $R = \exp(1/N) = e$ (e is the natural number) and a shape similar to the ellipse of modified Cam-Clay is obtained by adopting $R = \exp(1/N) = 2$.

Consider $\bar{\sigma}$ on the bounding surface as \bar{q} approaches 0 from the positive side such that $t = +1$. For the case that \bar{p}' approaches \bar{p}'_c it can be shown that: $\partial f / \partial p'$ approaches ∞ and $\mathbf{n} = [1, 0]^T$ for $N > 1$; $\partial f / \partial p'$ approaches $M_{cs} / \ln R$ for $N = 1$; and $\partial f / \partial p'$ approaches 0 and $\mathbf{n} = [0, 1]^T$ for $N < 1$. For the case that \bar{p}' approaches 0 it can be shown that $\partial f / \partial p'$ approaches $-\infty$ and $\mathbf{n} = [-1, 0]^T$ for all values of N . Similarly, as \bar{q} approaches 0 from the negative side such that $t = -1$ it can be shown that for the case that \bar{p}' approaches \bar{p}'_c : $\partial f / \partial p'$ approaches $-\infty$ and $\mathbf{n} = [1, 0]^T$ for $N > 1$; $\partial f / \partial p'$ approaches $M_{cs} / \ln R$ for $N = 1$; and $\partial f / \partial p'$ approaches 0 and $\mathbf{n} = [0, 1]^T$ for $N < 1$. For the case that \bar{p}' approaches 0 it can be shown that $\partial f / \partial p'$ approaches ∞ and $\mathbf{n} = [-1, 0]^T$ for all values of N . In summary, if $N > 1$ then the bounding surface remains smooth and continuous as it intersects the p' axis at right angles when $\bar{p}' = \bar{p}'_c$ (as $n_q = 0$). For $N < 1$ the bounding surface intersects the p' axis at a tangent when $\bar{p}' = \bar{p}'_c$ (as $n_p = 0$). Therefore, the constraint of $N > 1$ is imposed in this investigation and enables modelling of plastic strains during isotropic loading ($q = 0$), a feature lacking from the models of Manzari and Dafalias [32] and Gajo and Muir Wood [33].

4.6. Limiting isotropic compression line

Inherent in the definitions of the bounding surface and elasticity is the existence of a limiting isotropic compression line (LICL) in the v - $\ln p'$ plane, towards which the stress trajectories of all

isotropic compression load paths approach. It is for this reason that the CSL and LICL must be correctly defined at high stresses where particle crushing may occur even if high stresses are not of particular interest in the investigation at hand. For saturated conditions the LICL is expressed as

$$v = f_{cs} \left(\frac{p'}{R} \right) - \kappa \ln R \quad (15)$$

in which R represents the ratio between p'_c and p' at the critical state.

4.7. Plastic potential

A non-associated flow rule is assumed that ensures the plastic volumetric strains are zero at the critical state. Consideration is given to various plastic deformation mechanisms that dissipate energy. The dilatency, d , is expressed as

$$d = \frac{\dot{\varepsilon}_p^p}{\dot{\varepsilon}_q^p} = \frac{\partial g / \partial p'}{\partial g / \partial q} = (1 + k_d \xi) M_{cs} - \eta \quad (16)$$

where ξ is the state parameter [34] defined as the vertical distance between the current state and CSL in the v - $\ln p'$ plane. The state parameter is positive when the current state is above the CSL, is negative when the current state is below the CSL and is equal to zero when current state is at the critical state. $(1 + k_d \xi) M_{cs}$ controls the amount of energy dissipation. Equation (16) can be integrated to give the plastic potential $g = 0$. Then \mathbf{m} is defined by the general equation

$$\mathbf{m} = \frac{\frac{\partial g}{\partial \boldsymbol{\sigma}}}{\left\| \frac{\partial g}{\partial \boldsymbol{\sigma}} \right\|} = \left[\frac{td}{\sqrt[4]{1+d^2}}, \frac{t}{\sqrt[4]{1+d^2}} \right]^T \quad (17)$$

It is noted that the plastic potential does not intersect the p' axis at right angles and a discontinuity in the slope exists as q changes between slightly positive and slightly negative values. To avoid the development of plastic deviatoric strains during isotropic compression a smooth function for g that intersects the p' axis at right angles similar to f in Equation (13) could be adopted although would introduce additional material parameters. For simplicity, Equation (17) is preferred here and it is assumed that g is rounded off near the p' axis [35, p. 123] such that $\mathbf{m} = [1, 0]^T$ when $q = 0$.

By assuming energy is dissipated purely in friction, with a friction angle equal to that at the critical state, it can be assumed that $k_d = 0$ and the plastic potential of Cam-Clay is recovered. However, other energy dissipation mechanisms such as particle sliding, rotation and crushing must also be taken into account. The only restriction on $(1 + k_d \xi) M_{cs}$ is that it must be equal to M_{cs} at the critical state. However, for some soils, or when particularly high-precision simulations are not required, $k_d = 0$ may be an adequate assumption.

4.8. Hardening rules

The hardening modulus h is split into two components:

$$h = h_b + h_f \quad (18)$$

where h_b is the modulus at $\bar{\sigma}$ on the bounding surface. h_f is an arbitrary modulus at σ , defined as a function of the distance between $\bar{\sigma}$ and σ and is defined such that it attains a value of zero when $\bar{\sigma} = \sigma$.

It is assumed \bar{p}'_c undergoes isotropic hardening with changes in s as well as plastic volumetric strains, similar to the assumptions of Loret and Khalili [4, 22]. For collapsible soils, suction hardening occurs as a result of \bar{p}'_c increasing at a faster rate than \bar{p}' during an increase in s [15]. Then satisfying the consistency condition of the bounding surface, it follows that

$$h_b = - \frac{\partial F}{\partial \bar{p}'_c} \left(\frac{\partial \bar{p}'_c}{\partial \bar{e}_p^p} + \frac{\partial \bar{p}'_c}{\partial s} \frac{\dot{s}}{\dot{\bar{e}}_p^p} \right) \frac{m_p}{\left\| \frac{\partial F}{\partial \bar{\sigma}} \right\|} \quad (19)$$

More specifically, it is assumed that the LICL undergoes a suction-dependant shift $\gamma(s)$ along the κ line in the v - p' plane as illustrated in Figure 3. $\gamma(s)$ is positive, has units of stress, and subject to $\gamma(s) = 0$ when $s \leq s_e$, where s_e is the suction value separating saturated and unsaturated states. It is noted that hardening rules may be adopted such that s has a multiplicative effect or combined additive and multiplicative effect on the hardening parameter [22]. However, an additive rule is preferred here due to the ease of its implementation and simplicity of the corresponding hardening function. In this case, by recalling that the saturated LICL is defined by Equation (15), an expression for the unsaturated LICL is

$$v = f_{cs} \left(\frac{p' - \gamma(s)}{R} \right) - \kappa \ln \left(\frac{Rp'}{p' - \gamma(s)} \right) \quad (20)$$

The shift of the unsaturated LICL is accompanied by a shift of the unsaturated CSL, assuming R is a material constant, and the unsaturated CSL (Equation (9b)) is expressed as

$$v = \hat{f}_{cs}(p', s) = f_{cs} \left(p' - \frac{\gamma(s)}{R} \right) - \kappa \ln \left(\frac{p'}{p' - \gamma(s)/R} \right) \quad (21)$$

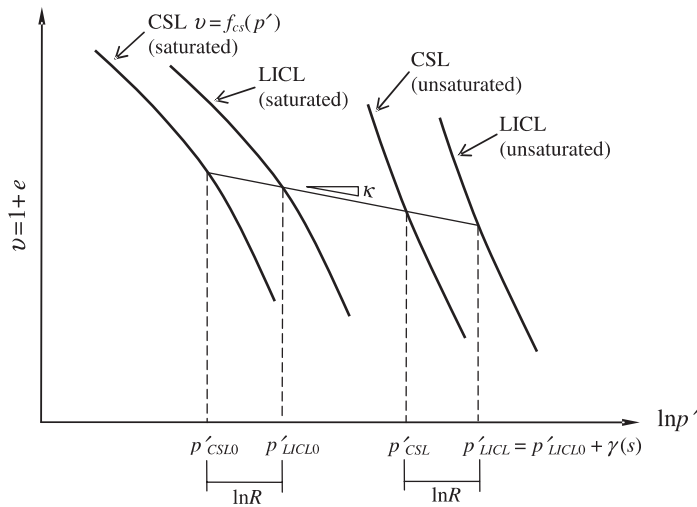


Figure 3. Saturated and unsaturated CSLs and LICLs in the v - $\ln p'$ plane.

Using the procedure outlined by Loret and Khalili [4, 22] it can be shown that the expression linking the plastic volumetric change (Δv^p) that occurs as the hardening parameter moves from the saturated LICL (\bar{p}'_{c1}) to the unsaturated LICL (\bar{p}'_{c2}) is

$$\Delta v^p = -(\bar{\lambda}^* - \kappa) \ln \left(\frac{\bar{p}'_{c2} - \gamma(s)}{\bar{p}'_{c1}} \right) \quad (22a)$$

$$\bar{p}'_{c2} = \bar{p}'_{c1} \exp \left[\frac{-\Delta v^p}{\bar{\lambda}^* - \kappa} \right] + \gamma(s) \quad (22b)$$

where $\bar{\lambda}^*$ is the slope of a straight line in the v - $\ln p'$ plane that connects the points \bar{p}'_{c1} and $\bar{p}'_{c2} - \gamma(s)$ on the saturated LICL. In the limit, Equation (22) becomes

$$\dot{\epsilon}_p^p = \frac{\lambda^* - \kappa}{v} \left(\frac{\dot{\bar{p}}'_c - \dot{\gamma}(s)}{\bar{p}'_c - \gamma(s)} \right) \quad (23a)$$

$$\dot{\bar{p}}'_c = \frac{v(\bar{p}'_c - \gamma(s))}{\lambda^* - \kappa} \dot{\epsilon}_p^p + \left(\frac{\partial \gamma(s)}{\partial s} \right) \dot{s} \quad (23b)$$

where λ^* is the slope of the saturated LICL in the v - $\ln p'$ plane at $\bar{p}'_c - \gamma(s)$. λ^* is therefore independent of $\gamma(s)$.

As indicated previously, h_f may take any arbitrary form provided it is equal to zero at $\boldsymbol{\sigma} = \bar{\boldsymbol{\sigma}}$. In the present study h_f is assumed to be of the form

$$h_f = k_m \frac{(\delta)}{(\delta_{\max} - \delta)} \frac{\Pi}{\bar{p}'_c} p' \quad (24)$$

where

$$\Pi = \frac{\partial \bar{p}'_c}{\partial \epsilon_p^p} + \frac{\partial \bar{p}'_c}{\partial s} \frac{\dot{s}}{\dot{\epsilon}_p^p} \quad (25)$$

and δ_{\max} and δ are the distances from the centre of homology located at $p' = q = 0$ and $\boldsymbol{\sigma} \rightarrow \bar{\boldsymbol{\sigma}}$, respectively, as shown in Figure 2. Note that if $(\delta_{\max} - \delta) \rightarrow 0$ then $h_f = \infty$ and if $\delta = 0$ then $h_f = 0$. Also, $k_m \geq 0$ is a scaling parameter controlling the steepness of the response in the q - ϵ_q plane. For some soils, or for a limited range of initial conditions, k_m may be a material constant. For other soils, or when particularly high-precision simulations are required, k_m may be defined as a function of initial conditions or changing state, based on the initial slope of the deviatoric response in the q - ϵ_q plane. The idea of defining parameters in the h_f component of the hardening modulus to depend on initial conditions or changing state is not an uncommon feature of bounding surface plasticity models [12, 13]. The ratio $\delta/(\delta_{\max} - \delta)$ may be written in the alternate form $(\bar{p}'_c - p'_c)/p'_c$ due to radial symmetry of the loading and bounding surfaces. The ratio Π/\bar{p}'_c introduces the similarity between h_f and h_b while p' provides a further scaling effect and gives h_f the dimension of stress. It can be seen that h_f is positive until it becomes zero at $\bar{p}'_c = p'_c$. Also, by denoting $(1 + k_d \xi)M_{cs}$ as M , it can be shown that h_b is positive for $\eta/M < 1$, negative for $\eta/M > 1$ and zero when $\eta = M$.

It is possible for h to become zero at some point when $\eta/M > 1$ where h_f and h_b are equal in magnitude and have opposite sign. At this point transition from hardening to softening occurs.

Such a situation is observed in the drained stress–strain behaviour of dense sands or heavily over-consolidated clays. However, if h_b and h remain positive, hardening will occur at all times. Such a situation is observed in the drained stress–strain behaviour of loose sands and normally or lightly over-consolidated clays. Additionally, h will become zero when the two requirements $\eta = M = M_{cs}$ and $p'_c = \bar{p}'_c$ are satisfied simultaneously. This situation occurs at the critical state.

Suction hardening rules of the type adopted here are able to account for volumetric collapse upon wetting as detailed by Loret and Khalili [4, 22]. In general terms, wetting causes a reduction in s and the hardening parameter is forced to retreat to the LICL corresponding to the lower value of s . Under a limiting confining pressure, this retreat is accompanied by a reduction in v .

4.9. Coupling the solid, air and water phases

If s is constant during soil deformation, the volume of water in the sample will vary, as will the volume of air. Conversely, s will vary during deformation if either the air or water volumes are held constant. It is therefore necessary to couple s with these volumes. The procedure for coupling the three phases of an unsaturated material in an effective stress framework is detailed by Khalili *et al.* [36] and the basic features are repeated here. Note that $v_w = S_r e$ is the specific pore water volume and $v_a = (1 - S_r)e$ is the specific pore air volume.

By adopting Betti's reciprocal rule it can be shown that for a material with incompressible grains [36]:

$$-\frac{\dot{v}_w}{v} = -\psi \frac{\dot{v}}{v} + [c'_m - \psi^2 c] \dot{s} \quad -\frac{\dot{v}_a}{v} = (\psi - 1) \frac{\dot{v}}{v} + [\psi^2 c - c'_m] \dot{s} \quad (26)$$

where $c = -(\partial v/v)/\partial p_n$ is the drained compressibility of the soil skeleton ($1/K$) when $\dot{s} = 0$, $c_m = -(\partial v/v)/\partial s$ is the compressibility of the soil skeleton with respect to s when $\dot{p}_n = 0$, c'_m is the compressibility of the water phase with respect to s and is dependant on the assumed soil water characteristic curve (SWCC) and $\psi = \partial(\chi s)/\partial s$.

5. MODEL CALIBRATION FOR UNSATURATED SPESWHITE KAOLIN

The results of a series of isotropic compression and triaxial shear tests on compacted speswhite kaolin in saturated and unsaturated states as reported by Wheeler and Sivakumar [2] are used in the model calibration here. These particular tests results have also been used by Loret and Khalili [4] to calibrate a conventional plasticity model and aspects of the calibration procedure adopted in that investigation as well as some of the material parameters are also adopted here. Specific details of experimental procedures and sample preparation are given in Wheeler and Sivakumar [2] and only the basic features are discussed here.

5.1. Test program

Samples 50 mm in diameter and 100 mm in height were prepared by compacting the soil at a moisture content of 25% into a mould in 9 equal layers. Each layer was statically compacted at a rate of 1.5 mm/min until a vertical stress of 400 kPa was achieved. The compaction procedure resulted in $v = 2.210$ and $S_r = 0.54$.

The samples were then transferred to a triaxial apparatus capable of supplying u_a to the top of the sample and u_w to the bottom of the sample. A high air entry filter was located

between the bottom of the sample and pore water supply. Suction was induced in a sample using the axis-translation technique as originally outlined by Hilf [37], in which a u_w smaller than u_a was applied, and the high air entry filter provided an air–water interface.

Samples were then subjected to $p_n = 50$ kPa and values of $s = 100$ kPa, 200 kPa and 300 kPa were established in the samples. v_w increased during this stage indicating that s was larger than 300 kPa immediately following compaction. A number of samples were also brought to a saturated state ($s = 0$) by supplying a lower u_a than u_w resulting in the upward flushing of water through the sample. During this stage, p_n reduced from 50 to 25 kPa. Finally, samples were isotropically compressed very slowly to a range of p_n values while holding s constant, during which time v reduced as did v_w indicating that the soil was undergoing drying. The samples were then sheared using a range of load paths.

SWCCs were not presented by Wheeler and Sivakumar [2] although Khalili and Khabbaz [38] were able to use the shear strength data at the critical state to back calculate the suction value separating saturated from unsaturated conditions as discussed below.

5.2. Material parameters

A saturated CSL that closely fits a single linear segment in the v – $\ln p'$ plane defined by $\lambda_0 = 0.125$ and $\Gamma_0 = 2.588$ (Figure 1) was found to be sufficient for speswhite kaolin. Also, Figure 4 presents the stresses q and p' at the end of the tests where critical state conditions were approached, in which the χ relationship of Khalili and Khabbaz [38]:

$$\chi = \left[\frac{s}{s_e} \right]^{-0.55} \quad (27)$$

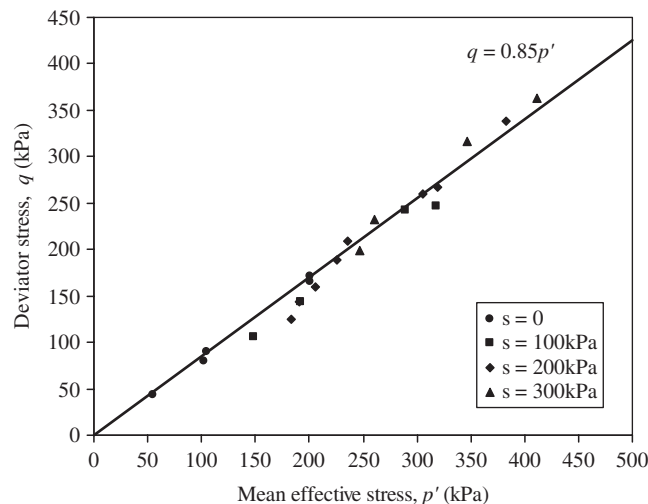


Figure 4. End points of a number of triaxial shear tests (performed by Wheeler and Sivakumar [2]) plotted in the q – p' plane during which critical state conditions were approached, conducted at constant suction, for speswhite kaolin.

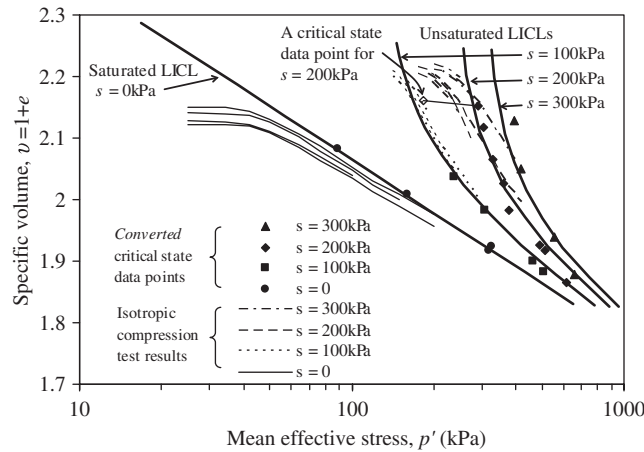


Figure 5. Results of isotropic compression tests, converted critical state data points (from Wheeler and Sivakumar [2]) and LICLs as adopted in the model (continuous bold lines) plotted in the v - $\ln p'$ plane.

was used to express stresses as effective. In this relationship s_e represents the suction value separating saturated from unsaturated conditions, and more specifically may be denoted using s_{ae} (air entry value) for a drying path and s_{ex} (air expulsion value) for a wetting path. A value of $s_e = s_{ae} = 85$ kPa (as back calculated by Khalili and Khabbaz [38] from shear strength data), and $M_{cs} = 0.85$ ($\phi'_{cs} = 21.9^\circ$) were found to fit the Wheeler and Sivakumar [2] data for both saturated and unsaturated conditions, Figure 4. It is noted that Equation (27) was established using suction ratios (s/s_e) less than 12. The validity of this relationship for fine-grained soils at larger suction ratios has not been tested. The elastic parameters were found to be $\kappa = 0.015$ and $\nu = 0.45$. The location of LICLs in the v - $\ln p'$ plane and their dependency on s were determined next. A number of isotropic compression test results from Wheeler and Sivakumar [2] are reproduced here in the v - $\ln p'$ plane in Figure 5. Also shown are the critical state data points converted to their corresponding value on the LICLs. To do this the p' value at each point was multiplied by some value of R and shifted along the κ line in the v - $\ln p'$ plane. The value of R was adjusted until the converted critical state data points plotted over the isotropic compression lines (LICLs). A value of $R = 1.6$ was found to be suitable. To illustrate this further consider the open diamond symbol in Figure 5 with co-ordinates (183, 2.16). This is one of the critical state data points for $s = 200$ kPa. The point was shifted along the κ line to the converted co-ordinate (293, 2.153). This was done for all the other data points for $s = 200$ kPa, and the bold continuous line that (approximately) passes through these points and forms an upper limit to the isotropic compression test results for $s = 200$ kPa becomes the LICL.

The suction dependant shift of the unsaturated LICLs from the saturated LICL in the v - $\ln p'$ plane in Figure 5 was defined by

$$\gamma(s) = \begin{cases} \left[45.11 \ln \left(\frac{s}{34} \right) \right]^{1.25} & \text{for } 100 \leq s \\ 128.5 \left(\frac{s - s_e}{100 - s_e} \right) & \text{for } s_e \leq s < 100 \end{cases} \quad (28)$$

indicating the presence of suction hardening. A value of $N = 1.4$ was found to be appropriate as it enabled a particularly good fit between the loading surface and results of the constant volume tests of Wheeler and Sivakumar [2] in the q - p' plane. These particular constant volume test results closely follow the loading surface and are therefore particularly sensitive to N as the initial states of samples are very close to the LICL and p'_c deviates only slightly from \bar{p}'_c . A suitable expression for k_d in the plastic potential was found by trial and error to be of the form

$$k_d = \frac{1.7}{\xi} \left\langle \left[1 - \frac{\gamma(s)}{\bar{p}'_c} \right] \exp \left(\frac{\xi}{\lambda_0 - \kappa} \right) + \frac{\gamma(s)}{\bar{p}'_c} - 1 \right\rangle \quad (29)$$

The symbol $\langle x \rangle$ is used such that $\langle x \rangle = x$ when $x > 0$ and $\langle x \rangle = 0$ when $x \leq 0$. The trial and error procedure involved fitting model simulations to experimental results, albeit for only lightly over-consolidated material. It is also noted that the function for k_d given here may vary for different soils. For some situations, such as when high-precision simulations are not essential, it may be acceptable to define k_d to be a material constant or equal to zero.

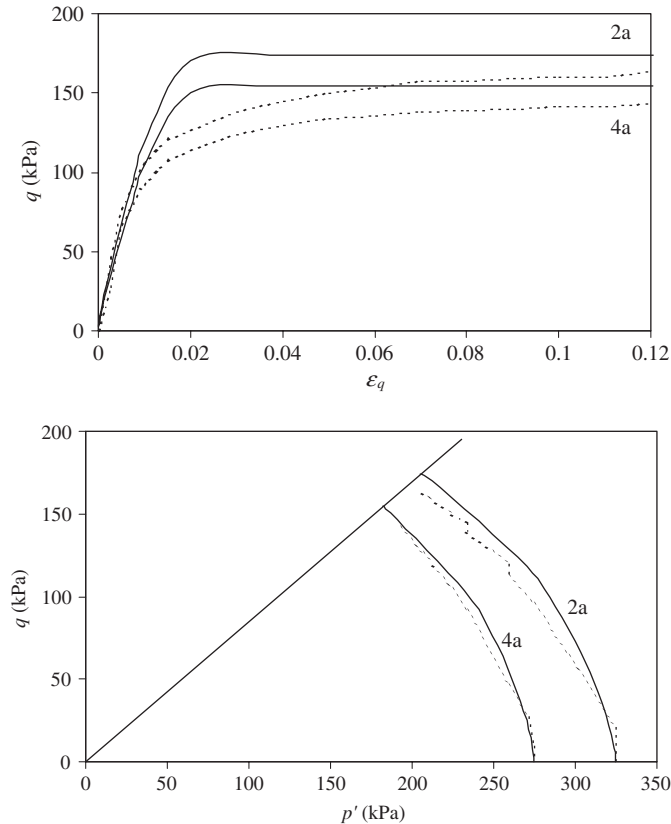


Figure 6. Experimental results and model simulations for triaxial compression tests on speswhite kaolin in which v and s were held constant. Initial conditions: $p_{n0} = 200$ kPa, $s_0 = 200$ kPa and $v_0 = 2.067$ (2a); and $p_{n0} = 150$ kPa, $s_0 = 200$ kPa and $v_0 = 2.127$ (4a).

The k_m parameter of the hardening modulus, again found by trial and error, was defined as

$$\log_{10} k_m = \left[1.45 \left(\frac{p'_0 R}{\bar{p}'_{c0}} \right) - 0.32 \right] \quad (30)$$

The subscript 0 denotes the initial condition of the subscripted variable. For some soils, or a limited range of initial conditions, k_m may become a material constant.

It is also noted that k_d and k_m were selected such that stress–strain behaviour *typical* of heavily over-consolidated material can be simulated, although further test results and comparisons with model simulations would be required to confirm the suitability of Equations (29) and (30) for such conditions.

5.3. Test results and theoretical simulations

The bounding surface plasticity model has been used to simulate some triaxial test results as shown here in Figures 6–8. The fit between simulation and experiment is a significant improvement compared to that achieved in other investigations (refer to References [2, 4])

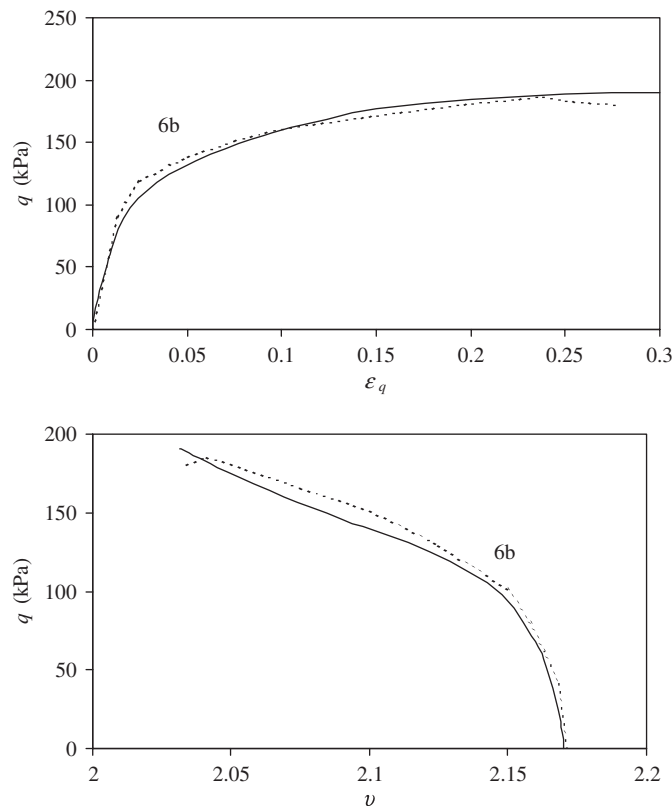


Figure 7. Experimental results and model simulations for a triaxial compression test on speswhite kaolin in which p_n and s were held constant. Initial conditions: $p_{n0} = 100$ kPa, $s_0 = 200$ kPa and $v_0 = 2.170$ (6b).

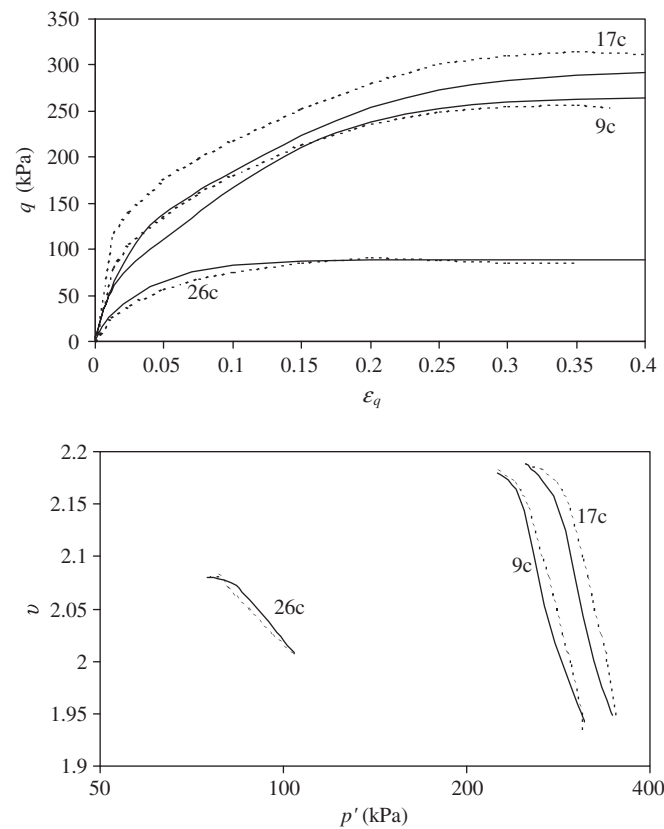


Figure 8. Experimental results and model simulations for triaxial compression tests on speswhite kaolin in which $\partial q/\partial p_n = 3$ and s was held constant. Initial conditions: $p_{n0} = 100$ kPa, $s_0 = 200$ kPa and $v_0 = 2.180$ (9c); $p_{n0} = 100$ kPa, $s_0 = 300$ kPa and $v_0 = 2.188$ (17c) and $p_{n0} = 75$ kPa, $s_0 = 0$ kPa and $v_0 = 2.080$ (26c).

involving the development of constitutive models using conventional Cam-Clay-based plasticity theory and calibrated using the same set of data. The improved fit highlights the versatility of bounding surface plasticity theory. The improvements are attributed to the definition of a more realistic loading direction (controlled by the loading surface) and plastic potential as compared to those obtained from the conventional Cam-Clay-based plasticity.

As the test results simulated here are for lightly over-consolidated samples a number of model simulations for saturated heavily over-consolidated samples are presented in Figure 9. The responses obtained are *typical* of those observed for heavily over-consolidated clays. Notably, the peak in the shear resistance for the most heavily over-consolidated samples ($v_0 = 1.78$ in Figure 9) is not excessively large, and the bounding surface plasticity model therefore overcomes one of the major limitations of the Cam-Clay-type models.

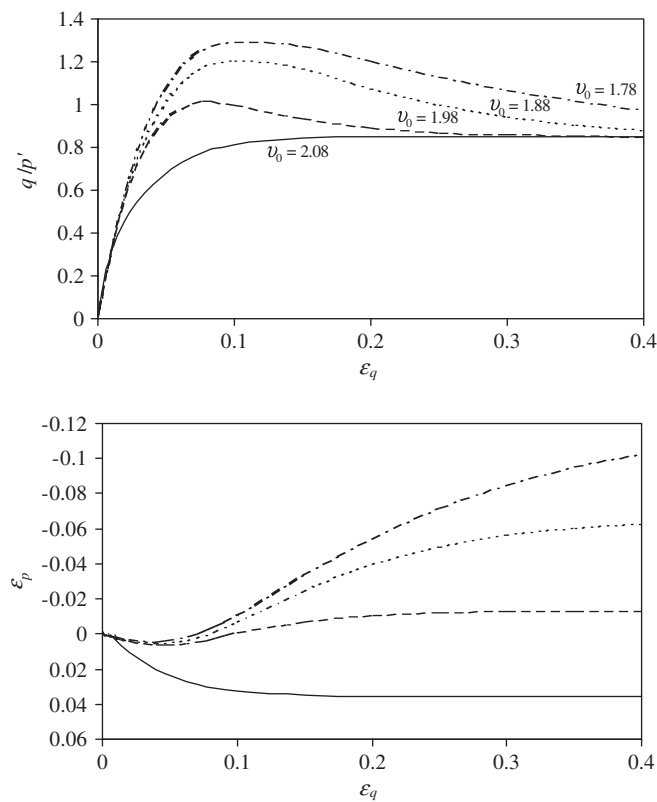


Figure 9. Model simulations for saturated drained triaxial compression tests subjected to constant σ'_3 with initial conditions $p'_0 = 75$ kPa, $v_0 = 2.08, 1.98, 1.88$ and 1.78 .

6. MODEL CALIBRATION FOR UNSATURATED KURNELL SAND

The model was calibrated for saturated Kurnell sand by Russell and Khalili [14] using a series of drained and undrained triaxial deviatoric tests, as well as isotropic and oedometric compression tests conducted at stress levels sufficient for particle crushing to occur, ranging from 10 to 15 000 kPa. Kurnell sand is predominantly quartz containing no fines and has the index properties $D_{50} = 0.31$ mm, $C_u = 1.83$, $G_s = 2.65$, $e_{\min} = 0.60$ and $e_{\max} = 0.92$. Presented here is an extension of this calibration for unsaturated Kurnell sand. Specific details of experimental procedures and sample preparation are given in Reference [16]. Only the basic features are discussed here.

6.1. Test program

Samples 50 mm in diameter and 51 mm in height were prepared by pluviation of the dry soil into a mould. Values of v ranging from 1.65 to 1.78 were achieved by adjusting the drop height. The samples were then saturated and transferred to a triaxial apparatus capable of supplying u_a to

the top of the sample and u_w to the bottom of the sample. Enlarged lubricated end platens were used. A high air entry ceramic disc (1515 kPa) was located between the bottom of the sample and pore water supply. Suction was induced in a sample using the axis-translation technique similar to that described previously. More specifically, the cell pressure and u_w were increased while maintaining a difference of about 10 kPa until cell pressure reached 600 kPa. The u_w connected to the top of the sample was then replaced with an equal u_a . The u_w connected to the bottom of the sample was then reduced to achieve the desired magnitude of s . Values of p_n ranging from 40 to 100 kPa and values of s ranging from 50 to 410 kPa were achieved.

Drained (constant s) tests were performed at a strain rate of 0.005 mm/min, sufficiently slow for water to enter or exit the sample and maintain constant s . Undrained (constant v_w) tests were conducted by testing at a strain rate of 0.25 mm/min. Most tests were performed beyond $\varepsilon_q = 0.4$ to obtain conditions as close as possible to the critical state. Corrections were made for the bedding error associated with the lubrication layer on the enlarged ends. Also corrections were made to the cell volume change measurements to account for creep of the Perspex triaxial cell and displacement of the loading platen. The effects of membrane penetration were considered in the investigation of Russell and Khalili [14]. Membrane effects were found to be significant only for the undrained triaxial tests performed on saturated sands. In fact, a *partial* drainage condition exists for these tests rather than an undrained condition. This is caused by changes in the amount of membrane penetration resulting from changes in effective stress across the membrane. The changes in membrane penetration are counteracted by changes in soil volume and pore water pressure and were accounted for [14]. However, the effects of membrane penetration are insignificant for undrained triaxial tests performed on unsaturated sands as the soil volume is able to change during such tests. It is only the pore water volume that is held constant. The changing membrane penetration that occurs is very small compared to changes in soil volume.

The oedometric compression tests on unsaturated samples were performed using a conventional front-loading oedometer and a custom designed and built fixed ring pressure cell. Each sample remained saturated while a mechanical axial load was applied in steps until a value of 57.4 kPa was achieved. This was then held constant while u_w was increased at the same rate as the chamber air pressure. u_w was then reduced and air pressure held constant to create a suction in the sample. Displaced pore water passed through the porous disc and its volume was monitored with time as was the vertical displacement of the loading yolk to determine when a state of equilibrium had been reached in the sample. This took about seven days. The mechanical loading was then increased in 24 kPa steps every two days.

The SWCC was determined using the pressure plate and filter paper techniques. Samples were prepared for testing to target values of v and tolerances of 1.68 ± 0.013 , 1.72 ± 0.015 and 1.78 ± 0.018 for both tests. The procedure detailed in ASTM D2325-68 for use of the pressure plate was generally followed in this investigation. Values of s as high as 1400 kPa were applied. A period of seven days was allowed after application of s for samples to reach equilibrium. For the filter paper tests, stacks of three oven dried Whatman No. 2 filter papers were placed on top of each sample and a small weight was placed on the stack to maintain good contact between it and sample as recommended by Swarbrick [39]. An airtight lid was then placed on the moulds that were then placed in a temperature and humidity controlled environment for a period of seven days. The moulds were then opened and the moisture content of the middle filter paper of the stack was then determined. Then, using a calibration curve that best fits those proposed in References [40–42], the s in the filter paper, and therefore the s in the sample were inferred.

6.2. Material parameters

Russell and Khalili [14] showed that the saturated CSL closely fits the three linear segments defined by $\lambda_0 = 0.0284$, $\Gamma_0 = 2.0373$, $v_{cr} = 1.835$, $\lambda_{cr} = 0.195$, $v_f = 1.25$ and $\lambda_f = 0.04$ along with the fitting parameters $F1 = -6.3$, $F2 = -0.022$, $F3 = 0.205$ and $F4 = -0.16$. Also, a slope $M_{cs} = 1.475$ corresponding to $\phi_{cs} = 36.3^\circ$ was found to fit the data well. The elastic parameters were found to be $\kappa = 0.006$ and $\nu = 0.3$ and values of $N = 3$ and $R = 7.3$ were found to be appropriate. A suitable expression for k_d in the plastic potential was of the form

$$k_d = \frac{[-9.6\zeta_0 - 4.1]\langle -\xi_0 \rangle + [23\zeta_0 + 3.4]\langle \xi_0 \rangle}{\zeta_0} \quad (31)$$

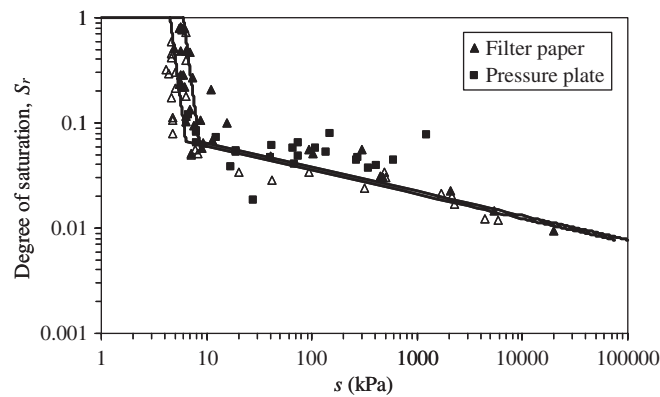


Figure 10. SWCC for Kurnell sand in the $\ln S_r$ - $\ln s$ plane. Bold symbols are for drying and hollow symbols are for wetting.

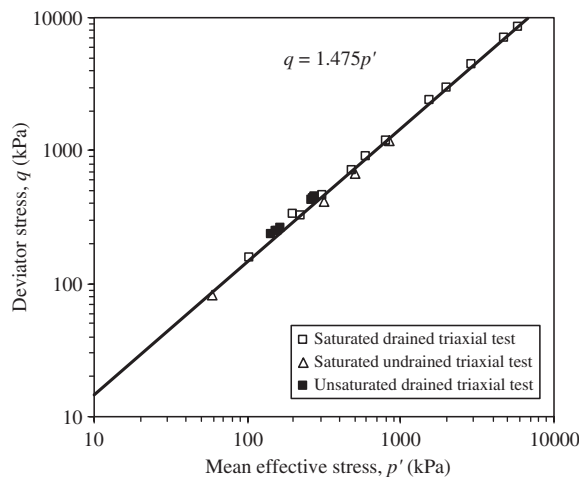


Figure 11. Triaxial shear test results for Kurnell sand at critical state.

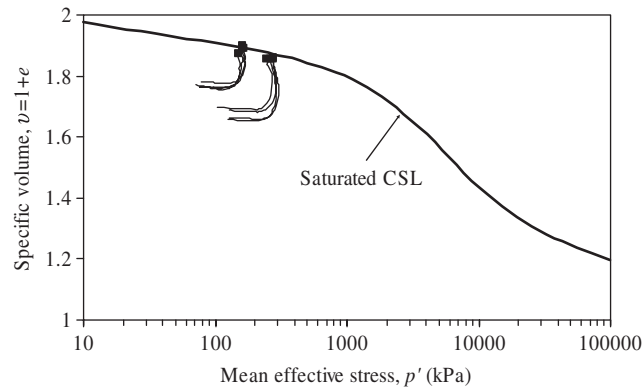


Figure 12. Stress Trajectories of unsaturated drained triaxial shear tests for Kurnell sand.

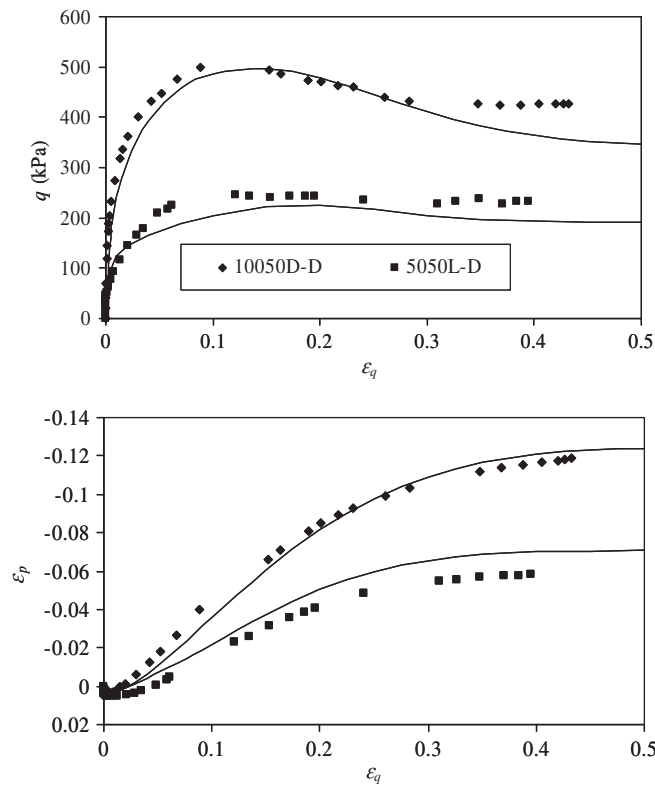


Figure 13. Experimental results and model simulations for triaxial compression tests on Kurnell sand in which $\partial q / \partial p_n = 3$ and s was held constant. Initial conditions: $p_{n0} = 50$ kPa, $s_0 = 51$ kPa and $v_0 = 1.770$ (5050L-D); and $p_{n0} = 102$ kPa, $s_0 = 51$ kPa and $v_0 = 1.658$ (10050D-D).

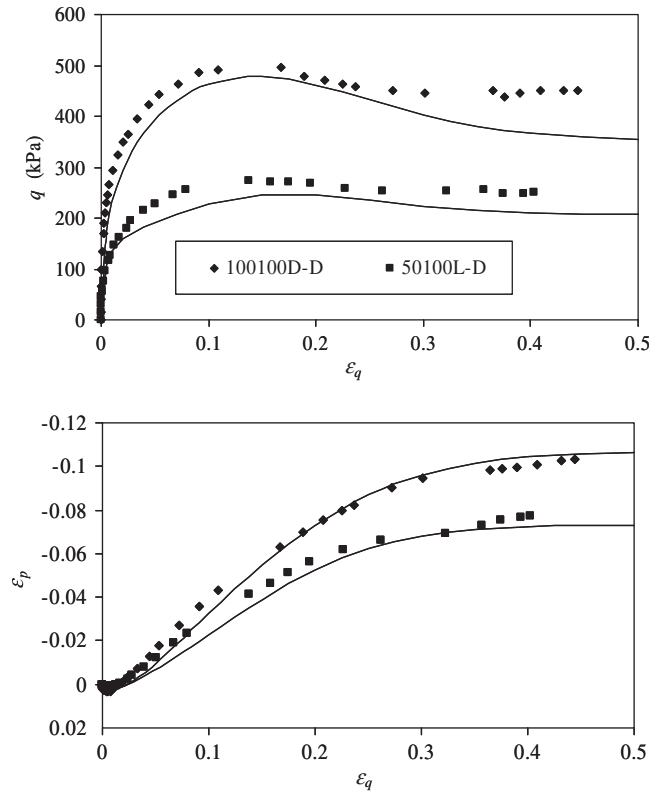


Figure 14. Experimental results and model simulations for triaxial compression tests on Kurnell sand in which $\partial q / \partial p_n = 3$ and s was held constant. Initial conditions: $p_{n0} = 50$ kPa, $s_0 = 100$ kPa and $v_0 = 1.763$ (50100L-D); and $p_{n0} = 100$ kPa, $s_0 = 100$ kPa and $v_0 = 1.687$ (100100D-D).

where ζ is the bounded state parameter of Russell and Khalili [14] defined as the vertical distance between the current state and LICL in the v - $\ln p'$ plane and is always negative. k_m , controlling the magnitude of h_f , was defined as

$$k_m = \frac{\langle 52 - 48 \exp(\zeta_0) \rangle (p'_0)^{0.44}}{1000} \quad (32)$$

Again, k_d and k_m have been defined to vary with initial conditions and were determined by trial and error while trying to fit model simulations with experimental results. For some soils, or a limited range of initial conditions, it may be acceptable to define k_m to be a material constant and k_d to be material constant or equal to zero.

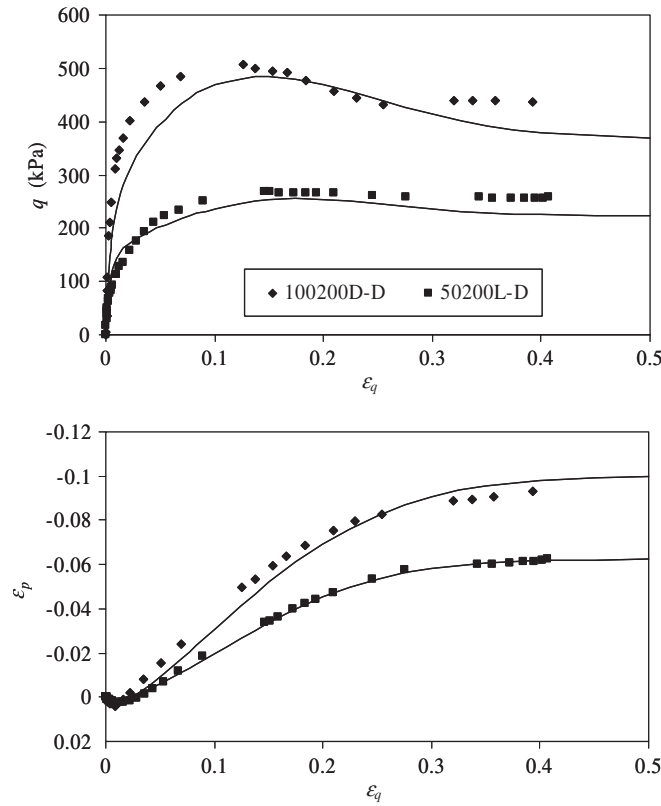


Figure 15. Experimental results and model simulations for triaxial compression tests on Kurnell sand in which $\partial q/\partial p_n = 3$ and s was held constant. Initial conditions: $p_{n0} = 51$ kPa, $s_0 = 198$ kPa and $v_0 = 1.780$ (50200L-D); and $p_{n0} = 101$ kPa, $s_0 = 200$ kPa and $v_0 = 1.697$ (100200D-D).

The SWCC was found to comprise three linear segments in the $\ln S_r - \ln s$ plane for all values of v tested and is expressed as

$$S_r = \begin{cases} 1.0 & \text{for } s \leq s_e \\ \left(\frac{s}{s_e}\right)^{-7.8} & \text{for } s_e < s \leq s_r \\ 0.0274G_s \left(\frac{s}{s_e}\right)^{-0.23} & \text{for } s_r < s \end{cases} \quad (33)$$

where s_e , as defined earlier, separates saturated from unsaturated states and represents the break between the first and second segments. s_r represents the break between the second and third segments, and $s_r = s_{rd}$ for a drying path and $s_r = s_{rw}$ for a wetting path.

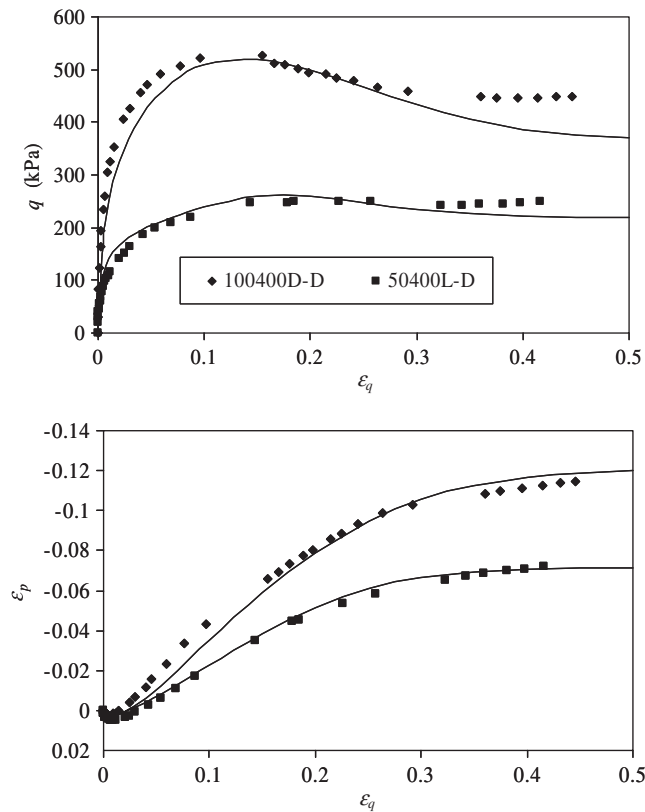


Figure 16. Experimental results and model simulations for triaxial compression tests on Kurnell sand in which $\partial q/\partial p_n = 3$ and s was held constant. Initial conditions: $p_{n0} = 50$ kPa, $s_0 = 400$ kPa and $v_0 = 1.764$ (50400L-D); and $p_{n0} = 100$ kPa, $s_0 = 400$ kPa and $v_0 = 1.663$ (100400D-D).

The SWCC is plotted in Figure 10. The solid symbols represent a drying path and the open symbols represent a wetting path. The SWCC is defined by $s_{ae} = 6.0$ kPa and $s_{rd} = 8.5$ kPa for drying and $s_{ex} = 4.5$ kPa and $s_{rw} = 6.4$ kPa for wetting. Note that a slight hysteresis exists between drying and wetting paths although the implications of this have not been explored in this investigation.

The end points of the unsaturated drained triaxial tests are presented in the $\ln q \sim \ln p'$ plane in Figure 11, along with a line of slope $M_{cs} = 1.475$ and the end points of the saturated triaxial tests from Russell and Khalili [14]. It can be seen that the unsaturated triaxial data lie within the same scatter as the saturated data, confirming $\phi'_{cs} = 36.3^\circ$ to be a material constant suited to saturated and unsaturated conditions. As can be seen in Figure 12, the trajectories for these tests approach the saturated CSL in the $v-\ln p'$ plane, indicating that the CSL is unique for saturated and unsaturated conditions and that no suction hardening occurs, i.e. $\partial \bar{p}'_c/\partial s = 0$ and $\gamma(s) = 0$. Note that in presenting the data in Figures 11 and 12 the effective stresses were calculated based on the χ relationship proposed Khalili and Khabbaz [38]

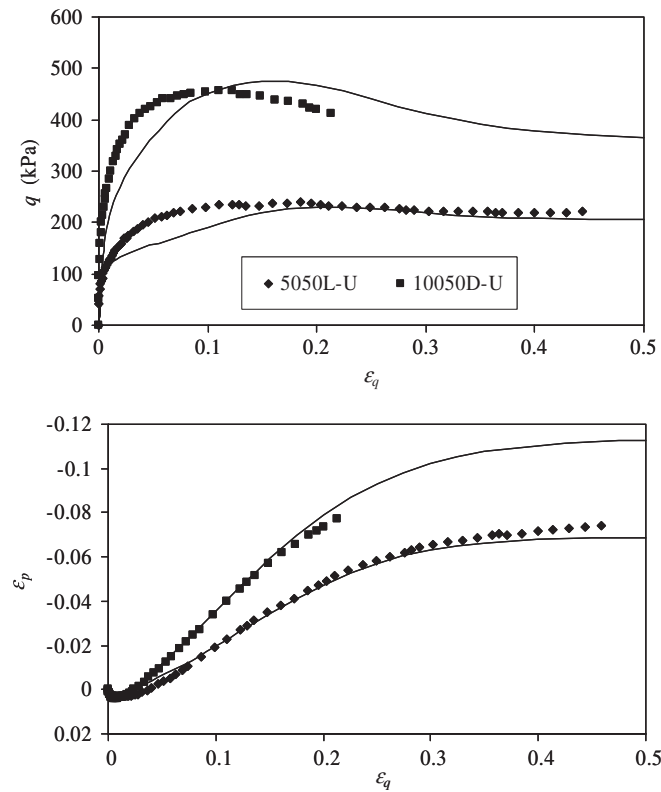


Figure 17. Experimental results and model simulations for triaxial compression tests on Kurnell sand in which $\partial q/\partial p_n = 3$ and v_w was held constant. Initial conditions: $p_{n0} = 50$ kPa, $s_0 = 50$ kPa and $v_0 = 1.771$ (5050L-U); and $p_{n0} = 100$ kPa, $s_0 = 50$ kPa and $v_0 = 1.676$ (10050D-U).

but with an extension to account for large suction ratios (s/s_e). Specifically, Khalili and Khabbaz [38] considered data points at suction ratios less than 12 in establishing the relationship for χ . However, in sands the value of s_e can be very small compared to s leading to suction ratios larger than 12. In fitting M_{cs} to the data it was found that χ needed to be changed for suction ratios larger than 25 according to

$$\chi = \begin{cases} \left(\frac{s}{s_e}\right)^{-0.55} & \text{for } \frac{s}{s_e} \leq 25 \\ 25^{0.45} \left(\frac{s}{s_e}\right)^{-1} & \text{for } \frac{s}{s_e} > 25 \end{cases} \quad (34)$$

Nevertheless, further laboratory tests results on silts and clays at suction ratios greater than 12 are required to establish the suitability of the extended relationship in (34) for a range of soil types.

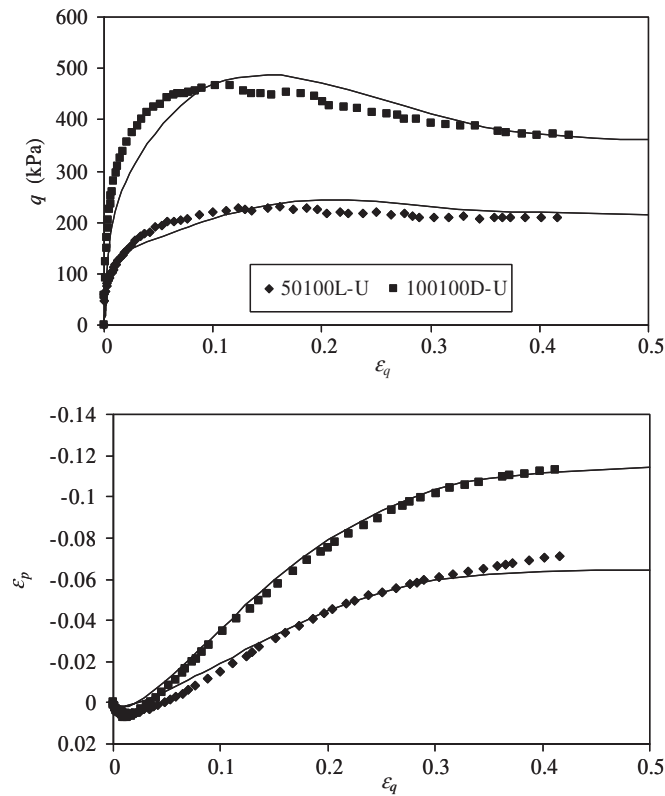


Figure 18. Experimental results and model simulations for triaxial compression tests on Kurnell sand in which $\partial q/\partial p_n = 3$ and v_w was held constant. Initial conditions: $p_{n0} = 49$ kPa, $s_0 = 98$ kPa and $v_0 = 1.777$ (50100L-U); and $p_{n0} = 98$ kPa, $s_0 = 100$ kPa and $v_0 = 1.674$ (100100D-U).

6.3. Test results and theoretical simulations

The material parameters given above for saturated conditions enable very accurate predictions of the stress–strain behaviour of Kurnell sand subjected to constant p' and constant σ'_3 drained triaxial compression, undrained triaxial compression, isotropic compression and oedometric compression across a wide range of stresses including those sufficient to cause particle crushing. The reader is referred to Reference [14] for details. Only predictions of unsaturated tests are presented in this investigation.

Figures 13–16 show the unsaturated drained triaxial test results and theoretical simulations in q – ε_q and ε_p – ε_q planes. Figures 17–20 show the unsaturated undrained triaxial test results and theoretical simulations in q – ε_q and ε_p – ε_q planes. There is a very good fit between simulation and experiment. Also, the stress–strain behaviour is analogous to that of saturated drained sands initially denser than critical. Specifically, hardening occurs up to a peak in the shear resistance, accompanied by initial volumetric contraction followed by volumetric expansion. Softening

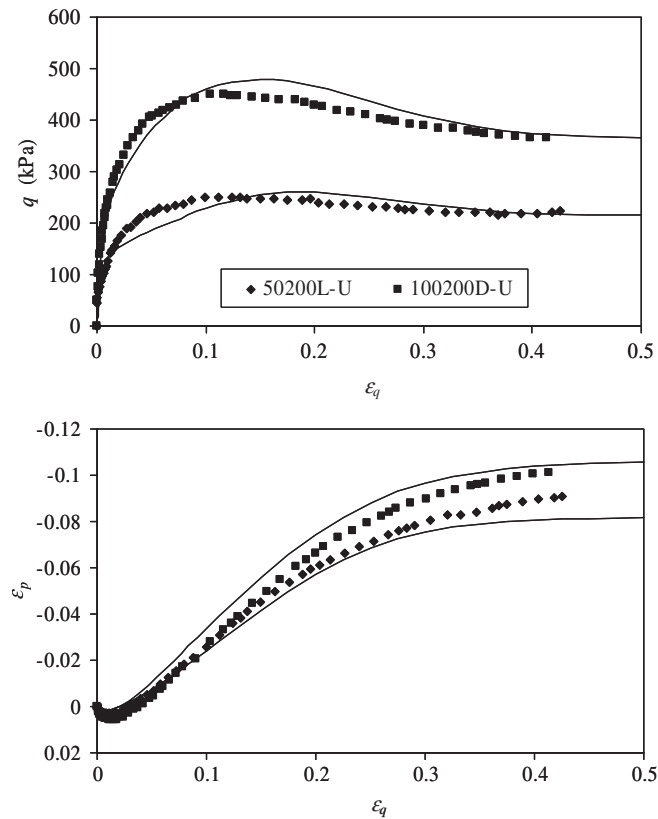


Figure 19. Experimental results and model simulations for triaxial compression tests on Kurnell sand in which $\partial q/\partial p_n = 3$ and v_w was held constant. Initial conditions $p_{n0} = 49$ kPa, $s_0 = 201$ kPa and $v_0 = 1.747$ (50200L-U); and $p_{n0} = 100$ kPa, $s_0 = 199$ kPa and $v_0 = 1.688$ (100200D-U).

towards the CSL is observed after reaching the peak and is accompanied by volumetric expansion. Note the much less pronounced peak is obtained from the use of enlarged lubricated ends.

Figure 21 shows the oedometric compression test results in v - $\ln \sigma_{1n}$ and v - $\ln \sigma'_1$ planes. A plot of σ_{3n}/σ_{1n} - $\ln \sigma'_1$ is also provided in Figure 22 for the oedometric compression tests. Again, a good fit is observed between simulation and experiment. Note that it was necessary to assume initial values in the simulations as the CSL is defined in a semi-logarithmic plane where zero stress level is undefined. Specifically, elastic strains and $\sigma'_3/\sigma'_1 = v/(1-v) = 0.429$ were assumed from $p' = 0$ to $p'_0 = 10$ kPa.

An important point regarding oedometric loading of unsaturated soils was made by Khalili *et al.* [15]. It is possible that s , which acts isotropically within the soil, may be sufficiently large such that σ_{3n} becomes zero, meaning that the soil separates from the confining ring and the condition of zero radial strain does not apply. This was checked through theoretical simulation

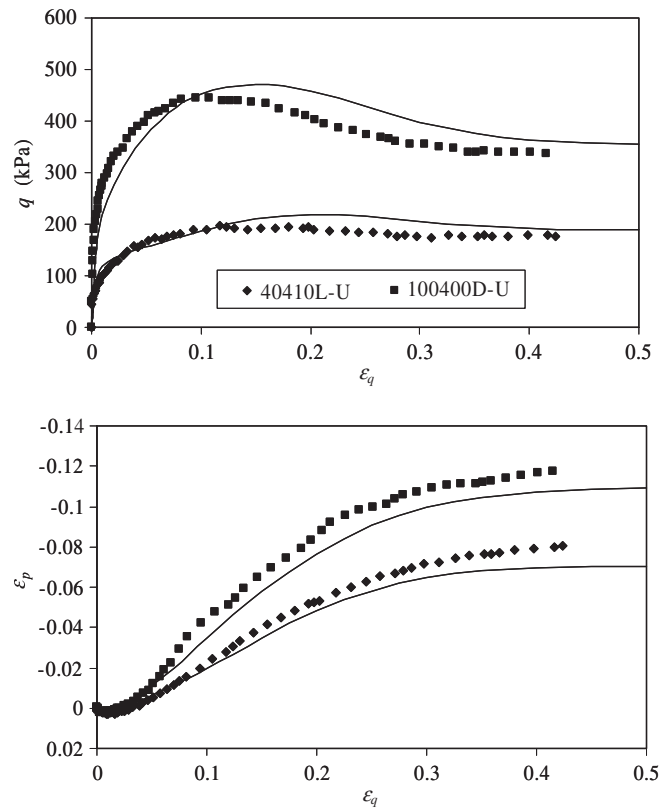


Figure 20. Experimental results and model simulations for triaxial compression tests on Kurnell sand in which $\partial q/\partial p_n = 3$ and v_w was held constant. Initial conditions $p_{n0} = 40$ kPa, $s_0 = 410$ kPa and $v_0 = 1.771$ (40410L-U); and $p_{n0} = 96$ kPa, $s_0 = 403$ kPa and $v_0 = 1.683$ (100400D-U).

and, as can be seen in Figure 22, σ_{3n} is always larger than 0 such that the zero radial strain of oedometric compression always applies. However, this behaviour may not be observed if s was applied at lower values of σ_{ln} , as σ_{3n} may become zero at which point the sample would separate from the confining ring.

7. CONCLUSIONS

This paper presents a simple bounding surface plasticity model in a critical state framework that is suited to describe the stress–strain behaviour of a wider range of unsaturated soils. This was made possible by using the concept of effective stress and adopting sufficiently general and versatile definitions for the basic model ingredients. More specifically, a simple isotropic elastic rule was adopted. Versatile functions for the loading surface and bounding surface were defined

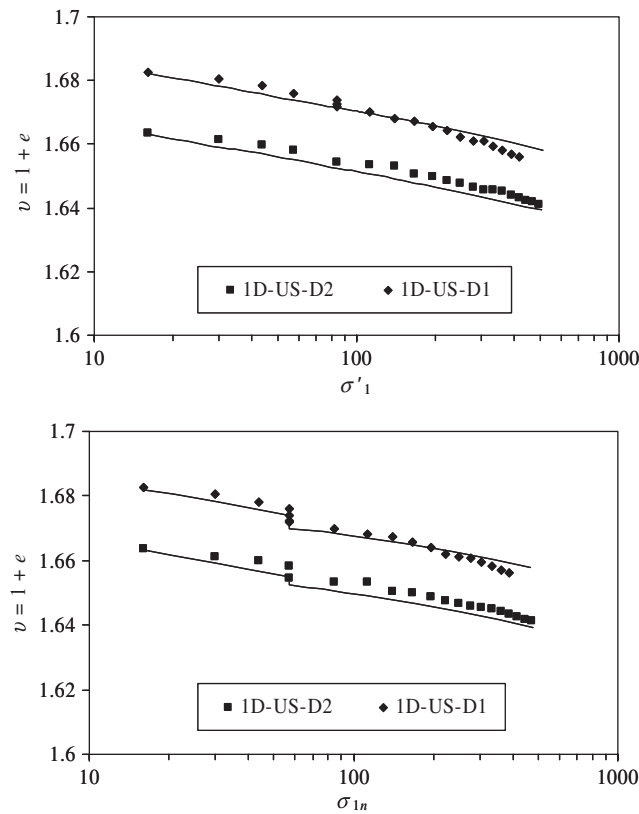


Figure 21. Experimental results and model simulations for oedometric compression tests on Kurnell sand in which s was held constant. Test conditions: $v_0 = 1.682$, $p'_0 = 10$ kPa and s increased from 0 to 600 kPa at $\sigma_{1n} = 57.4$ kPa (1D-US-D1); and $v_0 = 1.663$, $p'_0 = 10$ kPa and s increased from 0 to 200 kPa at $\sigma_{1n} = 57.4$ kPa (1D-US-D2).

that are able to describe the varied loading directions of different soils. A plastic potential was adopted that is of a general form suited to a range of soil types. A hardening modulus was defined that includes one component for isotropic hardening due to changes in plastic volumetric strains and suction and another component that is arbitrarily defined for any particular soil.

The models versatility was highlighted by its ability to simulate to high accuracy the stress–strain behaviour of unsaturated speswhite kaolin subjected to three triaxial test load paths and the stress–strain behaviour of unsaturated Kurnell sand subjected to two triaxial test load paths and the oedometric compression load path.

The effective stress parameter defined for Kurnell sand may well be a general definition for a wider range of soil types although requires validation for fine-grained soils and suction ratios larger than 12.

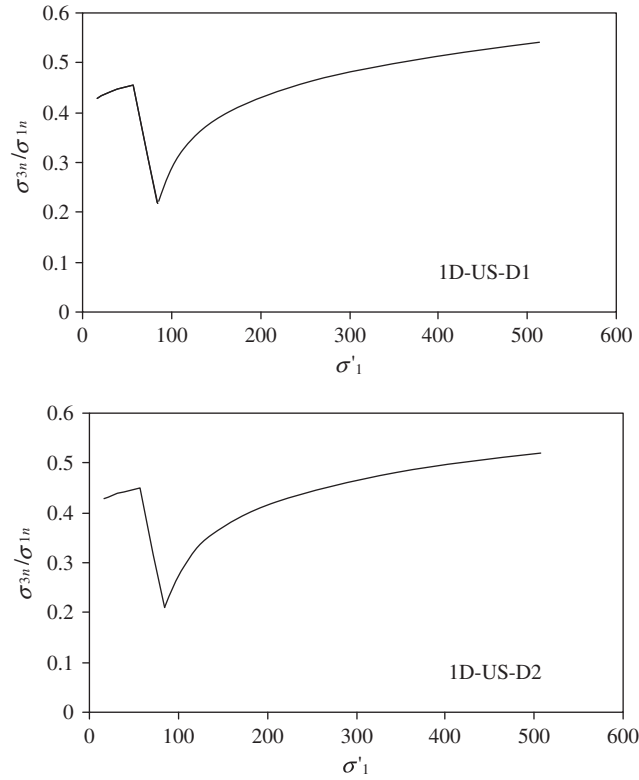


Figure 22. Model simulations for oedometric compression tests on Kurnell sand in which s was held constant. Test conditions $v_0 = 1.682$, $p'_0 = 10$ kPa and s increased from 0 to 600 kPa at $\sigma_{1n} = 57.4$ kPa (1D-US-D1); and $v_0 = 1.663$, $p'_0 = 10$ kPa and s increased from 0 to 200 kPa at $\sigma_{1n} = 57.4$ kPa (1D-US-D2).

APPENDIX A

A smooth and continuous function f_{cs} that closely fits the three linear segments of the CSL in Figure 1 is of the form:

$$v = a + b \tan^{-1}[c - d(\ln p' + F1)] + J(\ln p' + F1 - m)^3 + K(\ln p' + F1 - m)^2 + F2 \quad (A1)$$

where

$$\begin{aligned} a &= \frac{\hat{v}_{cr} + \hat{v}_f}{2}; & b &= \frac{\hat{v}_{cr} - \hat{v}_f}{\pi}; & c &= \frac{\pi \lambda_{cr}}{2(\hat{v}_{cr} - \hat{v}_f)} \left[2 \left(\frac{\Gamma_0 - \hat{v}_{cr}}{\lambda_0} \right) + \frac{\hat{v}_{cr} - \hat{v}_f}{\lambda_{cr}} \right] \\ d &= \frac{\lambda_{cr}}{b}; & m &= \frac{c}{d}; & J &= \frac{\lambda_0 - \lambda_f}{4m^2} - \frac{\Gamma_0 - \hat{v}_{cr}}{m^3}; & K &= \frac{\lambda_0 - \lambda_f}{4m} \\ \hat{v}_{cr} &= v_{cr} + F3; & \hat{v}_f &= v_f + F4 \end{aligned}$$

and $F1$, $F2$, $F3$ and $F4$ are fitting parameters.

It follows that the unsaturated CSL and LICL are defined by
CSL

$$v_{cs} = a + b \tan^{-1} \left[c - d \left(\ln \left(\bar{p}'_c - \frac{\gamma(s)}{R} \right) + F1 \right) \right] + J \left(\ln \left(\bar{p}'_c - \frac{\gamma(s)}{R} \right) + F1 - m \right)^3 \\ + K \left(\ln \left(\bar{p}'_c - \frac{\gamma(s)}{R} \right) + F1 - m \right)^2 + F2 - \kappa \ln \left(\frac{\bar{p}'_c}{\bar{p}'_c - \gamma(s)/R} \right) \quad (A2)$$

LICL

$$v_{LICL} = a + b \tan^{-1} \left[c - d \left(\ln \left(\frac{\bar{p}'_c - \gamma(s)}{R} \right) + F1 \right) \right] + J \left(\ln \left(\frac{\bar{p}'_c - \gamma(s)}{R} \right) + F1 - m \right)^3 \\ + K \left(\ln \left(\frac{\bar{p}'_c - \gamma(s)}{R} \right) + F1 - m \right)^2 + F2 - \kappa \ln \left(\frac{R\bar{p}'_c}{\bar{p}'_c - \gamma(s)} \right) \quad (A3)$$

REFERENCES

1. Alonso EE, Gens A, Josa A. A constitutive model for partially saturated soils. *Géotechnique* 1990; **40**(3):405–430.
2. Wheeler SJ, Sivakumar V. An elasto-plastic critical state framework for unsaturated soil. *Géotechnique* 1995; **45**(1):35–53.
3. Cui YJ, Delage P. Yielding and plastic behaviour of an unsaturated compacted silt. *Géotechnique* 1996; **46**(2): 291–311.
4. Loret B, Khalili N. An effective stress elastic–plastic model for unsaturated porous media. *Mechanics of Materials* 2002; **34**:97–116.
5. Gallipoli D, Gens A, Sharma R, Vaunat J. An elasto–plastic model for unsaturated soil incorporating the effects of suction and degree of saturation on mechanical behaviour. *Géotechnique* 2003; **53**(1):123–135.
6. Donald IB. Shear strength measurements in unsaturated non-cohesive soils with negative pore pressures. *Second Australia-New Zealand Conference on Soil Mechanics and Foundation Engineering, Christchurch, 1956*; 200–204.
7. Lee KL, Seed HB, Dunlop P. Effect of moisture on the strength of a clean sand. *Journal of the Soil Mechanics and Foundations Division (ASCE)* 1967; **93**(SM6):17–40.
8. Townner GD, Childs EC. The mechanical strength of unsaturated porous granular material. *Journal of Soil Science* 1972; **23**(4):481–498.
9. Rampino C, Mancuso C, Vinale F. Experimental behaviour and modelling of an unsaturated compacted soil. *Canadian Geotechnical Journal* 2000; **37**:748–763.
10. Jeffries MG. Nor-sand: a simple critical state model for sand. *Géotechnique* 1993; **43**(1):91–103.
11. Dafalias YF. Bounding surface plasticity: I. Mathematical foundation and hypoplasticity. *Journal of Engineering Mechanics (ASCE)* 1986; **112**(9):966–987.
12. Bardet JP. Bounding surface plasticity model for sands. *Journal of Engineering Mechanics (ASCE)* 1986; **112**(11):1198–1217.
13. Crouch RS, Wolf JP, Dafalias YF. Unified critical-state bounding-surface plasticity model for soil. *Journal of Engineering Mechanics (ASCE)* 1994; **120**(11):2251–2270.
14. Russell AR, Khalili N. A bounding surface plasticity model for sands exhibiting particle crushing. *Canadian Geotechnical Journal* 2004; **41**(6):1179–1192.
15. Khalili N, Geiser F, Blight GE. Effective stress in unsaturated soils, a review with new evidence. *International Journal of Geomechanics* 2004; **4**(2):115–126.
16. Russell AR. Cavity expansion in unsaturated soils. *Ph.D. Thesis*, The University of New South Wales, Australia, 2004.
17. Bishop AW. The principle of effective stress. *Teknisk Ukeblad* 1959; **106**(39):859–863.
18. Houlsby GT. The work input to an unsaturated granular material. *Géotechnique* 1997; **47**(1):193–196.
19. Been K, Jeffries MG, Hachey J. The critical state of sands. *Géotechnique* 1991; **41**(3):365–381.
20. Konrad JM. Sand state from cone penetrometer tests: a framework considering grain crushing stress. *Géotechnique* 1998; **48**(2):201–215.
21. Russell AR, Khalili N. Drained cavity expansion in sands exhibiting particle crushing. *International Journal for Numerical and Analytical Methods in Geomechanics* 2002; **26**:323–340.

22. Loret B, Khalili N. A three-phase model for unsaturated soils. *International Journal for Numerical and Analytical Methods in Geomechanics* 2000; **24**:893–927.
23. Lo KY, Roy M. Response of particulate materials at high pressures. *Soils and Foundations* 1973; **13**(1):61–76.
24. Lade PV. Elasto-plastic stress–strain theory for cohesionless soil with curved yield surfaces. *International Journal of Solids and Structures* 1977; **13**:1019–1035.
25. Colliat-Dangus JL, Desrues J, Foray P. Triaxial testing of granular soil under elevated cell pressure. In: *Advanced Triaxial Testing of Soil and Rock*, ASTM STP 977, Donaghe RT, Chaney RC, Silver ML (eds). ASTM: Philadelphia, 1988; 290–310.
26. Yamamuro JA, Lade PV. Drained sand behaviour in axisymmetric tests at high pressures. *Journal of Geotechnical Engineering* (ASCE) 1996; **122**(2):109–119.
27. Bellotti R, Ghionna V, Jamiolkowski M, Robertson PK, Peterson RW. Interpretation of moduli from self-boring pressuremeter tests in sand. *Géotechnique* 1989; **39**(2):269–292.
28. Wood DM. *Soil Behaviour and Critical State Soil Mechanics*. Cambridge University Press: Cambridge, 1990.
29. Dafalias YF, Popov EP. A model for nonlinearly hardening materials for complex loading. *Acta Mechanica* 1975; **21**:173–192.
30. Tatsuoka F, Ishihara K. Yielding of sand in triaxial compression. *Soils and Foundations* 1974; **14**(2):63–76.
31. Nova R, Wood DM. An experimental programme to define the yield function for sand. *Soils and Foundations* 1978; **18**(4):77–86.
32. Manzari MT, Dafalias YF. A critical state two-surface plasticity model for sands. *Géotechnique* 1997; **47**(2):255–272.
33. Gajo A, Muir Wood D. Severn-Trent sand: a kinematic-hardening constitutive model: the q – p formulation. *Géotechnique* 1999; **49**(5):595–614.
34. Been K, Jeffries MG. A state parameter for sands. *Géotechnique* 1985; **35**(2):99–112.
35. Zienkiewicz OC, Chan AHC, Pastor M, Schrefler BA, Shiomi T. *Computational Geomechanics with Special Reference to Earthquake Engineering*. Wiley: England, 1999.
36. Khalili N, Khabbaz MH, Valliappan S. An effective stress based numerical model for hydro-mechanical analysis in unsaturated porous media. *Computational Mechanics* 2000; **26**:174–184.
37. Hilf JW. An investigation of pore-water pressure in compacted cohesive soils. *Technical Memo 654*, US Bureau of Reclamation: Denver; 1956.
38. Khalili N, Khabbaz MH. A unique relationship for χ for the determination of the shear strength of unsaturated soils. *Géotechnique* 1998; **48**:681–687.
39. Swarbrick GE. Measurement of soil suction using the filter paper method. In *Proceedings of the 1st International Conference on Unsaturated Soils*, Alonso EE, Delage P (eds). A.A. Balkema: Rotterdam, 1995; 653–658.
40. Fawcett RG, Collis-George N. A filter-paper method for determining the moisture characteristics of soil. *Australian Journal of Experimental Agriculture and Animal Husbandry* 1967; **7**:162–167.
41. Hamblin AP. Filter-paper method for routine measurement of field water potential. *Journal of Hydrology* 1981; **53**:355–360.
42. Chandler RJ, Crilly MS, Montgomery-Smith G. A low-cost method of assessing clay desiccation for low-rise buildings. *Civil Engineering* (ICE) 1992; **92**:82–89.